



1 Mapping global leaf inclination angle (LIA) based on field 2 measurement data

3 Sijia Li^{1,2,3}, Hongliang Fang^{1,2}

4 ¹LREIS, Institute of Geographic Sciences and Natural Resources Research, Chinese Academy of Sciences, Beijing 100101,
5 China

6 ²College of Resources and Environment, University of Chinese Academy of Sciences, Beijing 100049, China

7 ³National-Local Joint Engineering Laboratory of Geo-Spatial Information Technology, Hunan University of Science and
8 Technology, Xiangtan 411201, China.

9 *Correspondence to:* Sijia Li (lisj.19b@igsnr.ac.cn)

10 **Abstract.** Leaf inclination angle (LIA), the angle between leaf surface normal and zenith directions, is a vital parameter in
11 radiative transfer, rainfall interception, evapotranspiration, photosynthesis, and hydrological processes. Due to the difficulty
12 in obtaining large-scale field measurement data, LIA is typically assumed to follow the spherical leaf distribution or simply
13 considered constant for different plant types. However, the appropriateness of these simplifications and the global LIA
14 distribution are still unknown. This study compiled global LIA measurements and generated the first global 500 m mean LIA
15 (MLA) product by gap-filling the LIA measurement data using a random forest regressor. Different generation strategies
16 were employed for noncrops and crops. The MLA product was evaluated by validating the nadir leaf projection function
17 ($G(0)$) derived from the MLA product with high-resolution reference data. The global MLA is $41.47^\circ \pm 9.55^\circ$, and the value
18 increases with latitude. The MLAs for different vegetation types follow the order of cereal crops (54.65°) > broadleaf crops
19 (52.35°) > deciduous needleleaf forest (50.05°) > shrubland (49.23°) > evergreen needleleaf forest (47.13°) \approx grassland
20 (47.12°) > deciduous broadleaf forest (41.23°) > evergreen broadleaf forest (34.40°). Cross-validation shows that the
21 predicted MLA presents a medium consistency ($r = 0.75$, $RMSE = 7.15^\circ$) with the validation samples for noncrops, whereas
22 crops show relatively lower correspondence ($r = 0.48$ and 0.60 for broadleaf crops and cereal crops) because of limited LIA
23 measurements and strong seasonality. The global $G(0)$ distribution is opposite to that of the MLA and agrees moderately
24 with the reference data ($r = 0.62$, $RMSE = 0.15$). This study shows that the common spherical and constant LIA assumptions
25 may underestimate the intercept capability for most vegetation. The MLA and $G(0)$ products derived in this study would
26 enhance our knowledge about global LIA and should greatly facilitate remote sensing retrieval and land surface modeling
27 studies.

28 The global MLA and $G(0)$ products can be accessed at:

29 Li, S. and Fang, H. 2024, <https://doi.org/10.5281/zenodo.10940673>.

30



31 1 Introduction

32 Vegetation regulates terrestrial carbon and water cycles through a series of biophysical processes such as photosynthesis,
33 respiration, and transpiration (Foley et al., 1996; Chen et al., 2019). These biophysical processes are mainly carried by leaves
34 and the characterization of leaves within canopies is vital for remote sensing and earth system modeling (Ross, 1975;
35 Lawrence et al., 2019). Leaf inclination angle (LIA) denotes the inclination of the leaf or needle to the horizontal plane or the
36 angle between the leaf surface normal and zenith (Wilson, 1960). LIA is a key canopy structural trait that determines
37 radiative transfer, rainfall interception, evapotranspiration, photosynthesis, and hydrological processes (Sellers, 1985; Ross,
38 1981; Mantilla-Perez and Salas Fernandez, 2017; Xiao et al., 2000; Maes and Steppe, 2012). LIA has been used in radiative
39 transfer modeling (RTM), remote sensing inversion, and land surface modeling (LSM) studies (Tang et al., 2016; Wang and
40 Fang, 2020; Lawrence et al., 2019; Ross, 1975).

41 At the canopy scale, the probability density of LIA or the fraction of leaf area per unit LIA is expressed as the leaf angle
42 distribution (LAD) (De Wit, 1965). De Wit (1965) summarized six theoretical LADs, including planophile, erectophile,
43 extremophile, plagiophile, uniform, and spherical distributions. Specifically, the spherical distribution assumes that the
44 relative probability density of the LIA is proportional to the area of the corresponding sphere surface element and its mean
45 leaf inclination angle (MLA) equals 57.3° ($MLA = 57.3^\circ$) (De Wit, 1965). Furthermore, Ross (1981) defined the inclination
46 index (χ_L) to describe the departure of LAD from the spherical distribution. For the planophile distribution, $\chi_L = 1$; for the
47 erectophile distribution, $\chi_L = -1$; and for the spherical distribution, $\chi_L = 0$. In the radiative transfer regime, LIA is generally
48 represented by the leaf projection function ($G(\theta)$), which is defined as the average projection ratio of unit leaf area in the
49 illumination or viewing direction θ (Ross, 1981; Nilson, 1971). The spherical distribution is characterized by an isotropic
50 leaf projection function ($G \equiv 0.5$) (De Wit, 1965).

51 In the field, LIA can be measured directly based on the leaf's geometrical structure or using indirect optical methods (Lang,
52 1973; Ryu et al., 2010; Norman and Campbell, 1989; Weiss and Baret, 2017). Using these methods, several LIA
53 measurements have been carried out and some LIA datasets were constructed (Kattge et al., 2020; Chianucci et al., 2018;
54 Hinojo-Hinojo and Goulden, 2020; Pisek and Adamson, 2020). These field methods are usually time-consuming and labor-
55 intensive and are typically difficult to acquire large-scale LIA (Li et al., 2023). In addition, the existing LIA datasets have
56 not been comprehensively analyzed. LIA has also been estimated from satellite imagery through empirical relationships or
57 radiative transfer model inversions (Zou and Mörtus, 2015; Bayat et al., 2018; Goel and Thompson, 1984). Remote sensing
58 methods are used primarily for crops in local regions, and the generality of these algorithms is limited (Li et al., 2023). Due
59 to the difficulty in large-scale LIA measurements and estimations, our knowledge about the global LIA remains lacking.

60 Because our understanding of the global LIA is limited, different LIA simplification strategies have been adopted in various
61 studies. For example, LIA is typically assumed to follow the spherical distribution (Tang et al., 2016; Zhao et al., 2020;
62 Wang and Fang, 2020). However, this assumption may decrease the accuracy of radiative transfer modeling, significantly
63 underestimate the radiation interception (Stadt and Lieffers, 2000), and cause large errors (>50%) in leaf area index (LAI)



64 measurements and inversions (Yan et al., 2021). The spherical LIA assumption may introduce greater error in the nadir
65 direction than other viewing geometries (Yan et al., 2021), considering the large G variation in this direction (Wilson, 1959).
66 The lack of global LIA knowledge also limits the retrieval of other vegetation structural parameters (Li et al., 2023). In many
67 LSMs, LIA is commonly treated as a fixed value for different plant function types (PFT) (Lawrence et al., 2019; Majasalmi
68 and Bright, 2019). Field LIA measurements have demonstrated that the spherical distribution is not appropriate for forests,
69 and the PFT-dependent LIA ignores LIA variation within the PFT (Pisek et al., 2013; Yan et al., 2021; Majasalmi and Bright,
70 2019).

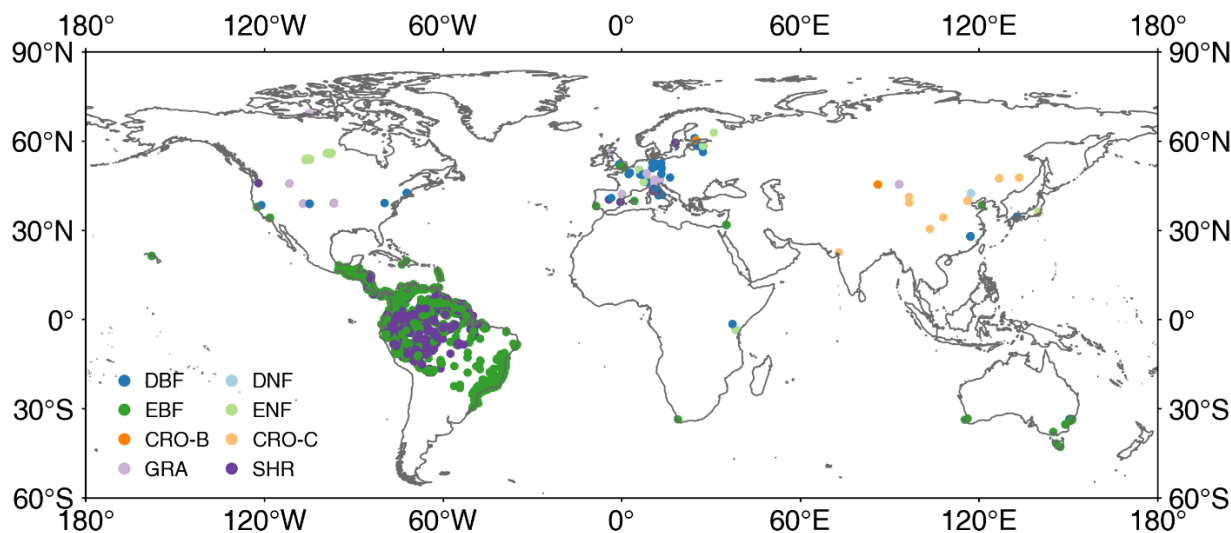
71 This study aims to generate the first global MLA map from existing LIA field measurements using a data-driven gap-filling
72 method. This method involves spatial expansion and upscaling of LIA measurements, and a random forest regressor using
73 input spectral, climate, and PFT data. Based on the global MLA map, we tested whether the spherical LIA assumption is
74 appropriate at the global scale. The new MLA map was validated by comparing the nadir G ($G(0)$) derived from the MLA
75 with high-resolution reference data. Section 2 outlines the materials and methods employed to generate and evaluate the
76 global MLA. Section 3 presents the global LIA measurements, global MLA and $G(0)$, and evaluation results. Section 4
77 discusses the performance of the global MLA and $G(0)$, the usage of the new MLA map, and the limitations of the study.
78 Section 5 presents the main conclusions.

79 2 Materials and methods

80 2.1 LIA measurement data

81 2.1.1 TRY LIA dataset

82 TRY is a network of vegetation scientists headed by Future Earth, the Max Planck Institute for Biogeochemistry, and
83 German Centre for Integrative Biodiversity Research, providing a global database of curated plant traits (the TRY database)
84 (<https://www.trydb.org/TryWeb/Home.php>). Since its establishment in 2007, the TRY database has continuously evolved
85 and has become one of the most widely used vegetation trait databases. The latest V6 version (released on October 13, 2022)
86 employed in this study contains 15,409,681 trait records covering 305,594 plant taxa (Kattge et al., 2020). In this database,
87 LIA was recorded as a numerical or categorical variable. After data extraction and checking, 31,043 valid records were used,
88 which include numerical LIA, locations, and species. Many measurements lack location information, whereas, for some
89 locations, there are many measurements for individual species. The spatial distribution map appears relatively sparse despite
90 a large volume of data (Fig. 1). The LIA measurements in South America are mainly from palms.



91
92 **Figure 1.** The locations of global leaf inclination angle measurements. DBF: deciduous broadleaf forest, DNF: deciduous needleleaf forest,
93 EBF: evergreen broadleaf forest, ENF: evergreen needleleaf forest, CRO-B: broadleaf crops, CRO-C: cereal crops, GRA: grassland, SHR:
94 shrubland.

95 2.1.2 LIA data from the literature

96 The LIA measurements in published literature were collected via keyword search (leaf angle, leaf inclination angle, and leaf
97 tilt angle) in the Web of Science, Google Scholar, Google, and Chinese documentary databases. The LIA, location, and
98 species information were manually extracted from the literature (Fig. 1). Several LIA measurements were already included
99 in the TRY database ([Chianucci et al., 2018](#); [Pisek and Adamson, 2020](#)). After aggregating LIA measurements for the same
100 species at the same location, 780 LIA records were accessed from previous studies ([Hinojo-Hinojo and Goulden, 2020](#); [Pisek](#)
101 [et al., 2022](#); [Chen et al., 2021](#)).

102 2.1.3 Manual LIA extraction

103 The majority of existing LIA measurements are located in the mid-latitudes of the Northern Hemisphere. Only a few
104 measurements in the northern tundra region were obtained, and the measurements in tropical regions are dominated by palm
105 trees (Fig. 1). Therefore, LIA data for the northern tundra and tropical regions were extracted from horizontal side-view
106 photographs searched from Google (Fig. S1).

107 ImageJ software (<https://imagej.nih.gov/ij/>) was used to process the leveled photographs and derive LIA following the
108 method of [Pisek et al. \(2011\)](#). The TRY species location data (848,919, Fig. S3b) (Jan 03, 2022) were used to obtain the
109 dominant species information in tropical rainforests and the northern tundra. For each species, more than 75 leaves
110 perpendicular to the viewing direction were selected and processed based on visual judgment to ensure the stability and
111 reliability of the MLA ([Pisek et al., 2013](#)). In total, the MLA of 104 species was manually derived.



112 In this study, most LIA measurements are obtained with protractor and level digital photogrammetry, especially for
 113 needleleaf species. Therefore, the distinction between branches and leaves is considered. The diverse LIA records from
 114 different sources were sorted to match the TRY species and to get the PFT based on the TRY Categorical Traits Dataset
 115 2018 (<https://www.try-db.org/TryWeb/Data.php#3>). The MLA was calculated for the LIA records with different forms. If
 116 there were multiple LIA records for the same species, the mean value was computed for the same location and species. In
 117 total, 5,554 LIA records of 1,194 species were collected, covering the growing season from 2001 to 2022. Considering the
 118 different numbers of records for each species, the LIA data was further aggregated by species.

119 2.2 Remote sensing data

120 2.2.1 Ancillary data used for MLA mapping

121 The ancillary data used for global MLA mapping and analysis are listed in Table 1. The PFT classification system in the
 122 MODIS global 500 m land cover type product (MCD12Q1.061) was used and mode-aggregated from 2001 to 2022 to match
 123 the LIA measurements (Fig. S2) ([Sulla-Menashe et al., 2019](#)). The 2001–2022 Landsat surface reflectance (Level 2,
 124 Collection 2, Tier 1) ([Crawford et al., 2023](#)), including Landsat 5 (2001–2012), Landsat 7 (2012–2013), and Landsat 8
 125 (2013–2022) was utilized to generate a global 30 m PFT map (Section 2.3.1), which was subsequently employed for LIA
 126 upscaling. The 2001–2022 MODIS bidirectional reflectance distribution function (BRDF) model parameters dataset
 127 (MCD43A1 C6.1) ([Schaaf and Wang, 2015a](#)) and nadir BRDF adjusted reflectance dataset (MCD43A4 V6 NBAR) ([Schaaf
 128 and Wang, 2015b](#)) are produced daily using 16 days of Terra and Aqua MODIS data at 500 m resolution and were utilized as
 129 predictive variables. Due to the scarcity of crop LIAs and the lack of location information for existing crop LIA
 130 measurements, fine-resolution (10/30 m) crop-type maps (Table 1) in 2018 were employed to support crop LIA mapping.
 131 Other data include the ERA5-Land reanalysis data, the ALOS digital elevation model (AW3D30 V3.2), and the 2001–2022
 132 MODIS LAI product (MCD15A2H) ([Myneni, 2015](#)). The LAI product was averaged and aggregated from 2001–2022. Most
 133 earth observation data were accessed and processed in Google Earth Engine (GEE) (<https://earthengine.google.com/>).

134

135 **Table 1.** Remote sensing data for global MLA mapping. BRDF: bidirectional reflectance distribution function.

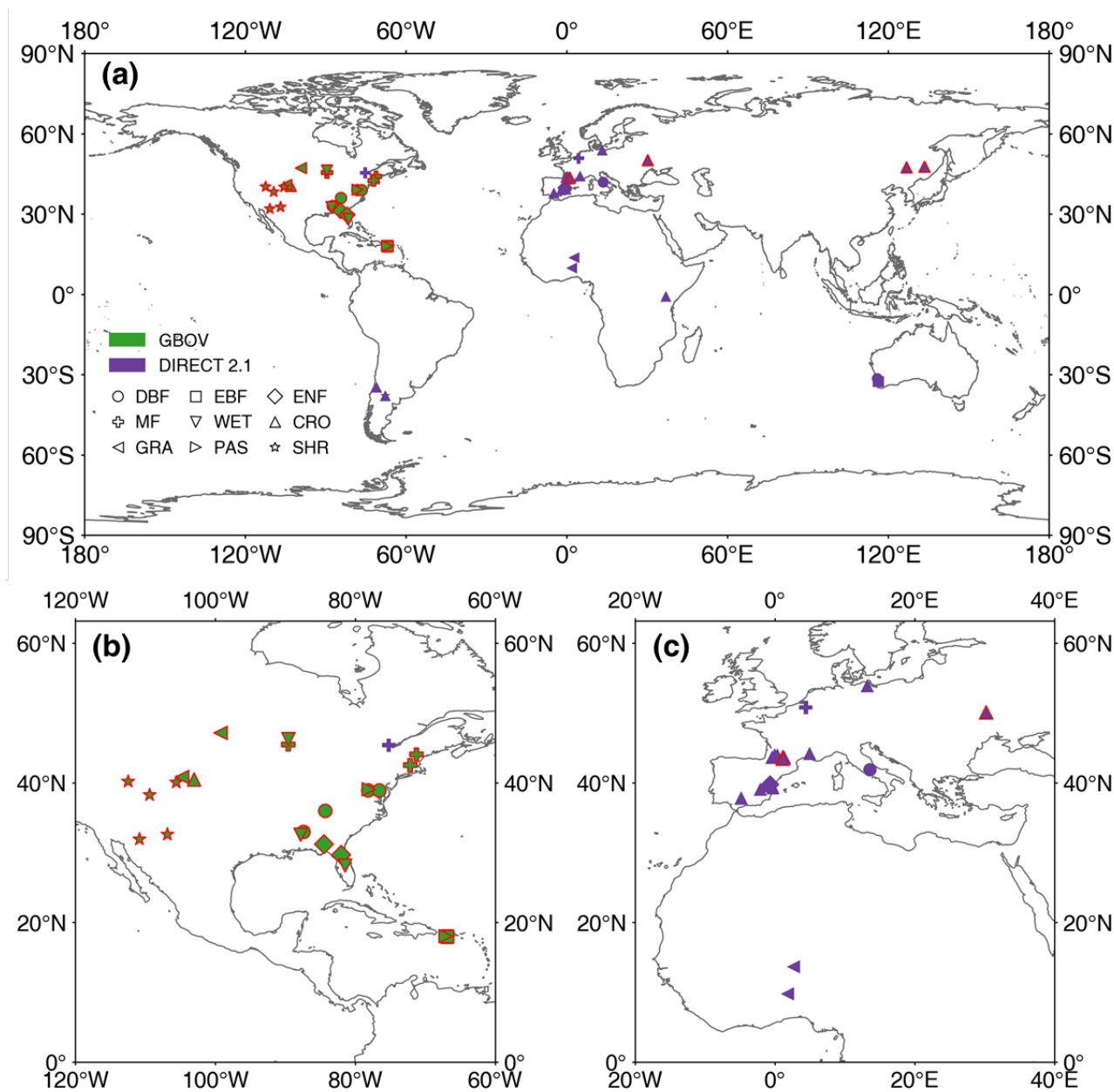
Category	Data	Year	Spatial resolution	Temporal resolution	Reference
Plant function type	MCD12Q1 C6	2001–2022	500 m	Yearly	(Sulla-Menashe et al., 2019)
Surface reflectance	Landsat collection 2	2001–2022	30 m	16 days	(Crawford et al., 2023)
	MCD43A4 V6 NBAR	2001–2022	500 m	Daily	(Schaaf and Wang, 2015b)
BRDF	MCD43A1 C6.1	2001–2022	500 m	Daily	(Schaaf and Wang, 2015a)
	Cropland Data Layers (CDL)	2018	30 m	Yearly	(Boryan et al., 2011)
Crop type	EUCROPMAP	2018	10 m	Yearly	(D’andrimont et al., 2021)
	AAFC Annual Crop Inventory	2018	30 m	Yearly	(Fisette et al., 2013)
	Northeast China crop-type	2018	30 m	Yearly	(You et al., 2021)



	map				
	NESEA-Rice10	2018	10 m	Yearly	(Han et al., 2021)
	China maize map	2018	30 m	Yearly	(Shen et al., 2022)
	China winter wheat map	2018	30 m	Yearly	(Dong et al., 2020)
Climate	ERA5-Land	2001–2022	0.1°	Monthly	(Muñoz-Sabater et al., 2021)
Terrain	AW3D30 V3.2	—	30 m	—	(Tadono et al., 2014)

136 2.2.2 High-resolution reference data

137 The high-resolution reference datasets provided by Ground Based Observations for Validation (GBOV,
138 <https://land.copernicus.eu/global/gbov/dataaccessLP/>) and DIRECT 2.1 (<https://calvalportal.ceos.org/lpv-direct-v2.1>) were
139 used to evaluate the generated global MLA (Fig. 2). These datasets provide high-resolution (20/30 m) LAI, effective LAI
140 (LAI_e), and fractional vegetation cover (FVC) data over a 3 km × 3 km area centered on each site generated using empirical
141 relationships between various vegetation indices and ground measurements ([Li et al., 2022](#); [Brown et al., 2020](#)). GBOV has
142 provided continuous high-resolution reference data since 2013 (Fig. 2).



143

144 **Figure 2.** Locations of GBOV and DIRECT 2.1 sites used in this study (a). (b) and (c) show the sites in North America and Europe,
145 respectively. CRO: Cultivated crops, MF: Mixed forest, PAS: Pasture/hay, WET: Woody wetlands. See Fig. 1 for other acronyms. The red
146 frame indicates those sites with >5 continuous records.



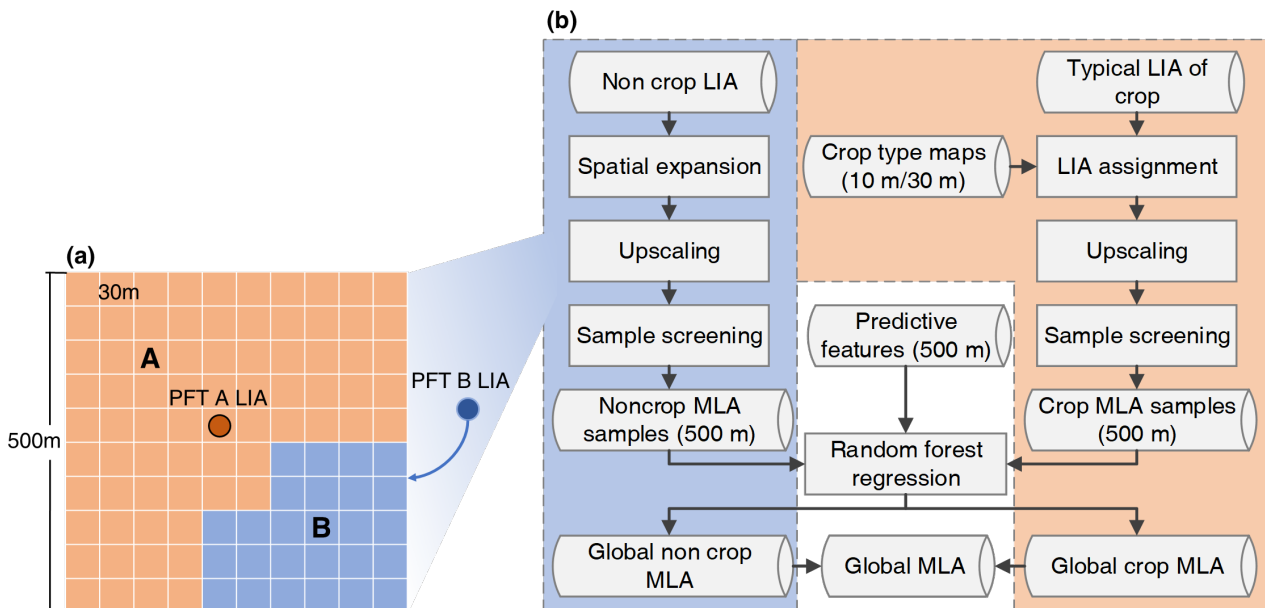
147 **2.3 Mapping global LIA**

148 **2.3.1 Data preparation**

149 Assuming equal LIA for the same species (Pisek et al., 2022; Toda et al., 2022; Raabe et al., 2015), the spatial coverage of
 150 LIA measurements was expanded, and those records without location information were utilized. Under this assumption, the
 151 LIA measurements were expanded through TRY species location data with species name matching. When a species had
 152 multiple LIA observations at different locations, the nearest LIA was assigned to the TRY species location. Visual
 153 inspections were conducted to remove potential TRY location biases, especially for non-vegetated points such as water
 154 bodies and deserts. After spatial expansion, the number of LIAs reached 12,328 (Fig. S3c).

155 In this study, the scale gap between field measurements and satellite remote sensing data was fully considered. To upscale
 156 the LIA measurements to the satellite resolution (500 m), a 30 m PFT map was first derived from Landsat reflectance using a
 157 random forest classification method. The random forest was trained at a 500 m scale using the mode-aggregated MODIS
 158 PFT classification map as training samples to generate a 30 m PFT map by hierarchically selecting homogeneous pixels
 159 (with a coefficient of variation < 0.2). The classification features were the same as those in the MODIS classification
 160 algorithm (Sulla-Menashe et al., 2019). For a 500 m pixel with multiple PFTs (Fig. 3a), when one PFT had no LIA
 161 measurement, the LIA of the PFT was assigned with the value of its nearest neighbor within 100 km with the same PFT. The
 162 500 m MLA was computed as the weighted average of the enhanced vegetation index (EVI2).

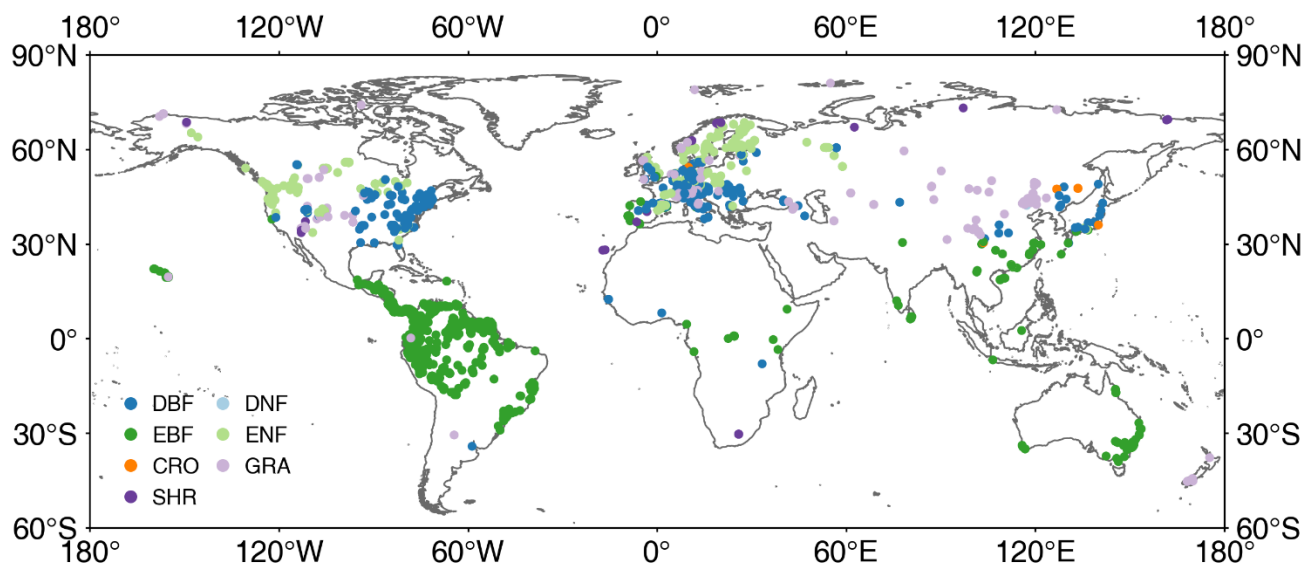
163
$$MLA_{500m} = \frac{\sum MLA_{30m} \times EVI2_{30m}}{\sum EVI2_{30m}} \quad (1)$$



164
 165 **Figure 3.** Leaf inclination angle (LIA) upscaling (a) and global mean LIA (MLA) mapping (b) strategies.



166 The 500 m upscaled MLA samples were further refined to select the most representative samples following three criteria: 1)
167 the coefficient of variation of the 30 m EVI2 in the 500 m pixel is less than 0.2, 2) the vegetation proportion in the 500 m
168 pixel is greater than 0.8, and 3) the proportion of PFTs represented by the MLA measurements in the 500 m pixel is greater
169 than 0.4. The final number of samples after refinement is 3,013 (Fig. 4).



170

171 **Figure 4.** Distribution of global mean leaf inclination angle samples after screening. See Fig. 1 for acronyms.

172 2.3.2 Global MLA mapping

173 Different mapping strategies were employed for noncrops and crops (Fig. 3b) considering the small number of valid crop
174 samples (Fig. 4) and the lack of location information for most crop samples. For noncrops, the upscaled 500 m MLA
175 samples were used to train a random forest regressor to predict the global MLA from different features (Table 2). To reduce
176 computational complexity and potential overfitting, a feature selection process was conducted based on the variable
177 importance (the sum of the decrease in Gini impurity index over all trees in the forest) computed by the model, and only the
178 40 most important variables were used in the final prediction. During the training process, the out-of-bag error was
179 minimized to obtain the optimal hyperparameters. The prediction performance of the random forest regressor was evaluated
180 using a ten-fold cross-validation approach.

181 For crops, the measured MLA values were averaged for different crop types as a typical MLA (Table S2). After assigning
182 typical MLAs for different crops with high-resolution crop maps (Table 1), the high-resolution crop MLA were upscaled to
183 500 m as training samples (Eq. (1)). Only the samples with a crop area ratio > 80% within a 500 m pixel were selected for
184 training. The crops were further divided into broadleaf crops and cereal crops and processed with the same procedure used
185 for noncrops (Fig. 3b). All procedures were conducted on GEE under the WGS-84 geographic coordinate system.

186



187 **Table 2.** Predictive features in global MLA mapping.

Category	Features	Variables	Number
Spectral	Blue, green, red, near-infrared reflectance	10%, 33%, 50%, 67%, 90% quantiles and standard deviation	24
	NDVI	10%, 33%, 50%, 67%, 90% quantiles and standard deviation	6
BRDF	Kernel coefficients of the red band	10%, 33%, 50%, 67%, 90% quantiles and standard deviation	18
	Kernel coefficients of near-infrared band	10%, 33%, 50%, 67%, 90% quantiles and standard deviation	18
Climate	PFT	Constant	1
	Solar downward radiation	Mean and standard deviation	2
	Temperature	Mean and standard deviation	2
Terrain	Precipitation	Mean and standard deviation	2
	Elevation	Constant	1
	Slope	Constant	1
	Aspect	Constant	1

188 **2.4 Evaluation of global MLA**

189 The global MLA map was indirectly evaluated using the leaf projection function, limited by the lack of high-resolution
 190 reference MLA. The global $G(0)$ was derived from the MLA and evaluated with high-resolution reference following the
 191 upscaling scheme recommended by the Land Product Validation (LPV) Subgroup of the Committee on Earth Observation
 192 Satellites (CEOS) (<http://lpvs.gsfc.nasa.gov/>). The nadir $G(0)$ is important considering that most satellite sensors adopt the
 193 nadir observation geometry.

194 Assuming a single-parameter ellipsoidal leaf angle distribution (Campbell, 1990), the parameter χ , the ratio of the horizontal
 195 and vertical axes of an ellipsoid, was first derived from MLA.

$$196 \chi = -3 + \left(\frac{MLA}{9.65}\right)^{-0.6061} \quad (2)$$

197 The $G(\theta)$ value in the nadir direction ($\theta=0^\circ$) was calculated using the following analytical formula.

$$198 G(\theta) = \frac{\sqrt{(\chi^2 + \tan^2 \theta) \cos \theta}}{\chi + 1.774(\chi + 1.182)^{-0.73}} \quad (3)$$

199 The reference $G(0)$ was derived from high-resolution LAI, FVC, and clumping index (CI) (=LAIe/LAI) with the Beer-
 200 Lambert law (Fig. S4) (Nilson, 1971).

$$201 P(\theta) = \exp \frac{G(\theta) + LAI + CI(\theta)}{\cos(\theta)} \quad (4)$$

202 Where $P(\theta)$, $CI(\theta)$, and $G(\theta)$ denote the gap fraction, CI, and G in direction θ , respectively. Specifically, the gap fraction in
 203 the nadir direction can be expressed by FVC.

$$204 P(0) = 1 - FVC \quad (5)$$



205 Therefore, the reference $G(0)$ was derived using the following formula.

$$206 \quad G(0)_{CI(0)} = -\frac{\ln(1-FVC)}{CI(0)*LAI} \quad (6)$$

207 By using the whole CI as the nadir CI ($CI(0)$) in the above equation (Fang et al., 2021; Li et al., 2022), $G(0)$ was calculated
208 as follows:

$$209 \quad G(0)_{CI} \approx -\frac{\ln(1-FVC)}{CI*LAI} \quad (7)$$

210 The MLA product was first upscaled to 3 km through a weighted averaging method using the MODIS LAI to derive $G(0)$
211 (Eq. (3)). The reference LAI, FVC, and CI were also upscaled to 3 km through simple averaging to compute the reference
212 $G(0)$ (Eq. (7)). The MLA-derived $G(0)$ and the reference $G(0)$ were compared at the 3 km \times 3 km area around each site. The
213 correlation coefficient (r), bias, and root mean square error (RMSE) were calculated as the evaluation metrics, as follows:

$$214 \quad r = \sqrt{1 - \frac{\sum_{i=1}^n (\hat{y}_i - y_i)^2}{\sum_{i=1}^n (y_i - \bar{y})^2}} \quad (8)$$

$$215 \quad Bias = \frac{1}{n} \sum_{i=1}^n (\hat{y} - y_i) \quad (9)$$

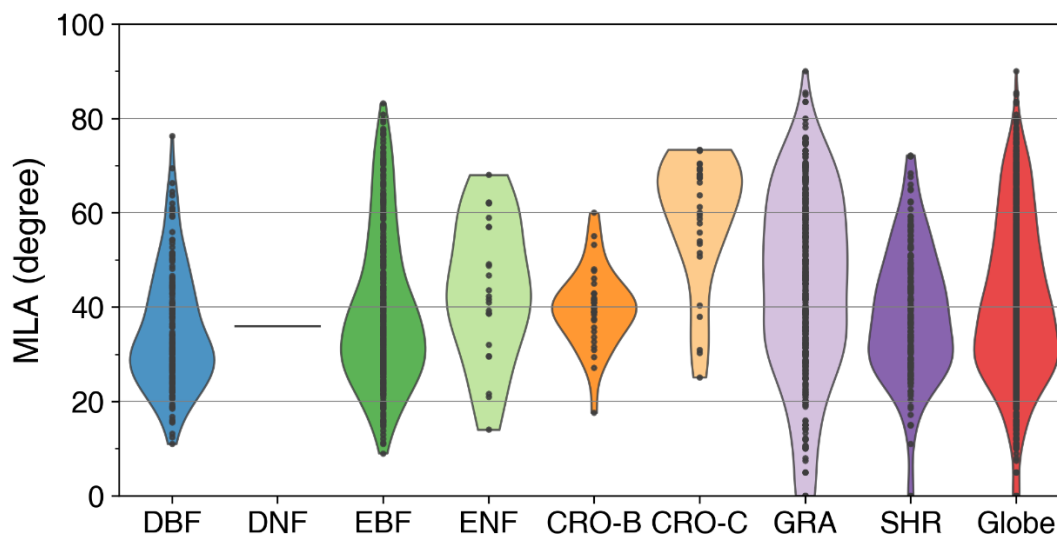
$$216 \quad RMSE = \sqrt{\frac{1}{n} \sum_{i=1}^n (\hat{y} - y_i)^2} \quad (10)$$

217 where \hat{y}_i , y_i , and n denote the MLA-derived $G(0)$, reference $G(0)$, and the number of $G(0)$, respectively.

218 3 Results

219 3.1 Global measured LIA values

220 The species-aggregated LIA was employed in the analysis of global LIA measurements. Fig. 5 shows the distributions of
221 global measured LIA values for different PFTs. The global measured MLA is 40.74° and generally follows the order of
222 CRO-C > GRA > ENF > CRO-B > EBF > SHR > DNF > DBF (Table 3). Cereal crops exhibit the highest MLA (59.11°),
223 whereas DBF has the most horizontal leaves (MLA = 34.94°). GRA and EBF show large LIA variations (Std = 20.44° and
224 17.17°), whereas CRO-B exhibits a small range. The DNF LIA measurements are only for one species and show very little
225 variation (Fig. 5).



226

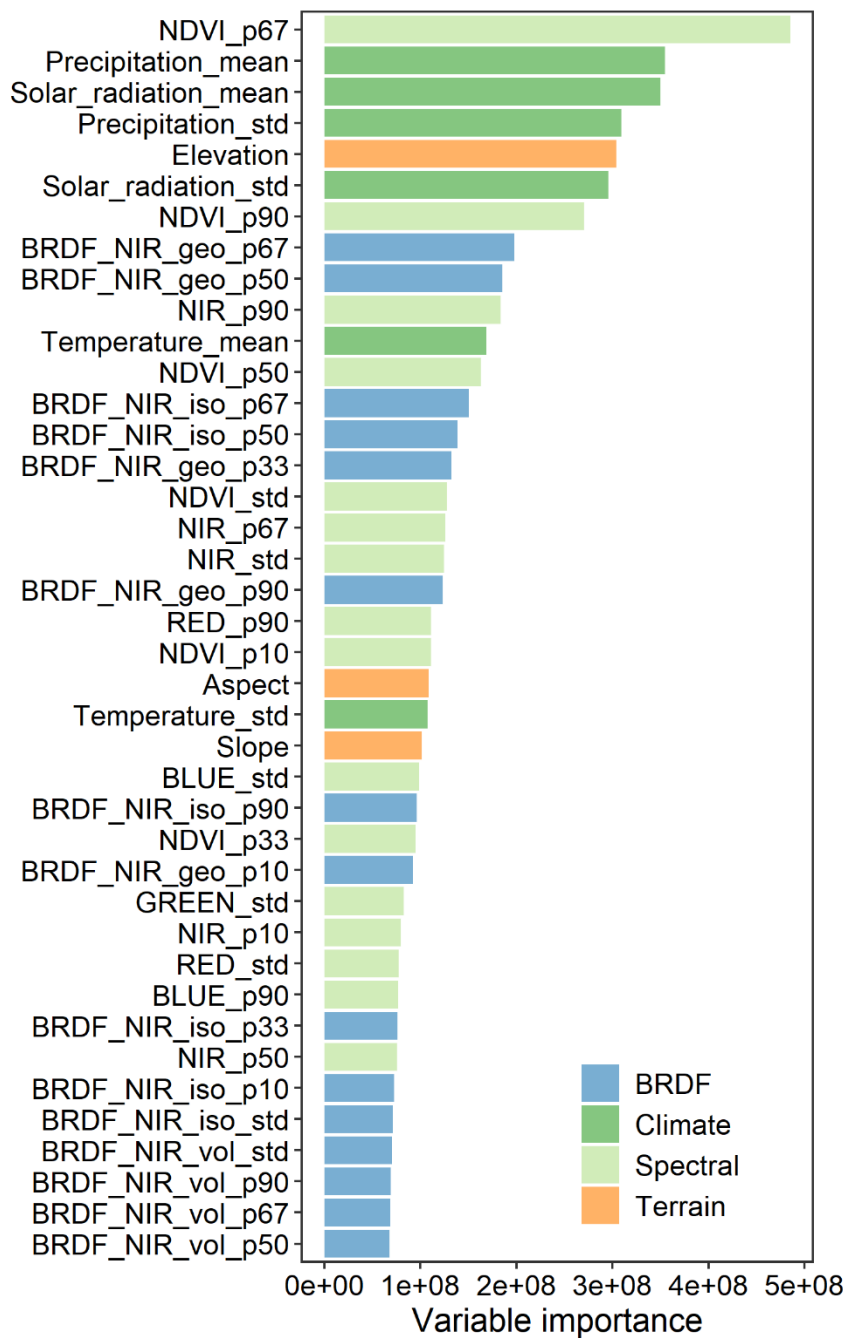
227 **Figure 5.** Distribution of global mean LIA (MLA) for different plant function types (see Fig. 1 for acronyms). The last shape shows the
 228 global average. Statistics are conducted for each species as represented by points in the figure.

229 **Table 3.** Statistics of leaf inclination angle measured for different plant functional types (PFT). STD is the standard deviation. The
 230 inclination index (χ_L) is converted from mean leaf inclination angle (MLA) ($\chi_L = 2\cos(\text{MLA}) - 1$) (Lawrence et al., 2019).

PFT	DBF	DNF	EBF	ENF	CRO-B	CRO-C	GRA	SHR	Globe
Number of species	171	1	347	23	32	31	399	190	1194
Mean(°)	34.94	35.88	39.30	43.69	39.71	59.11	44.13	38.32	40.74
STD (°)	12.40	0.00	16.11	14.40	8.11	13.28	20.17	13.80	17.12
χ_L	0.64	0.62	0.55	0.45	0.54	0.03	0.44	0.57	0.52

231 **3.2 The relationships between MLA and other variables**

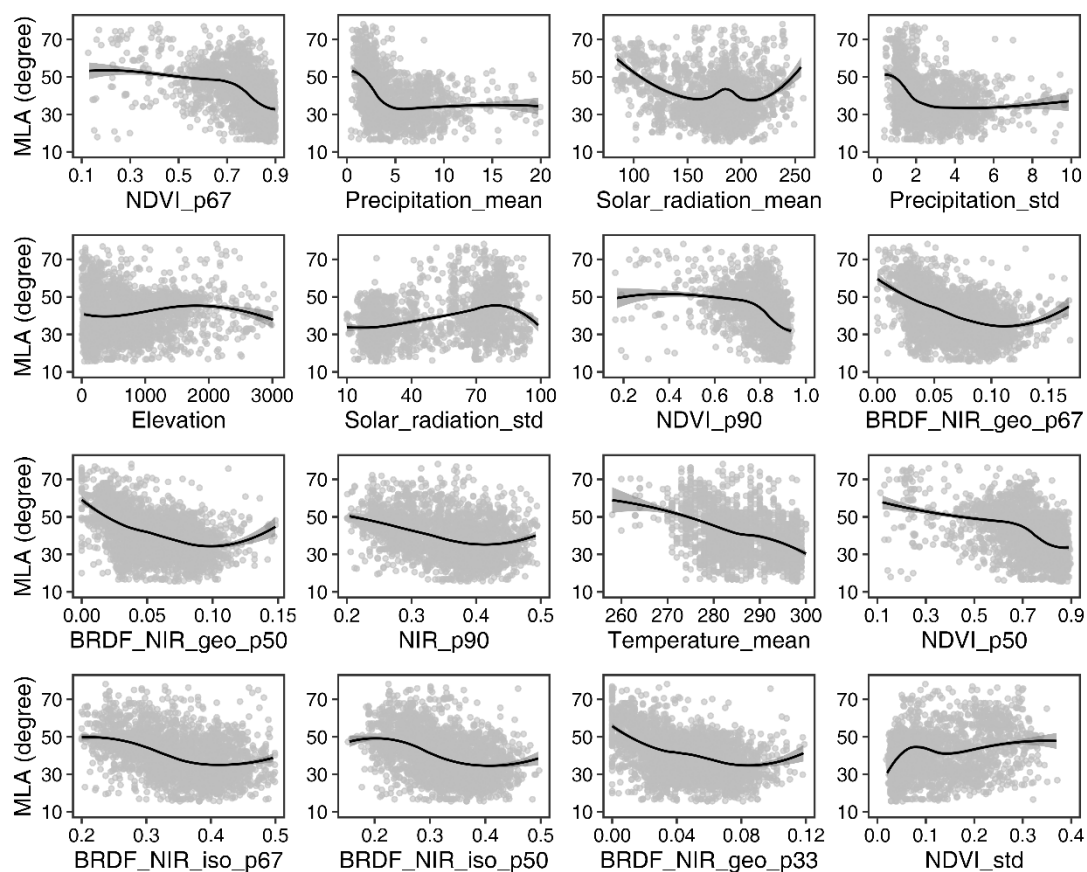
232 Fig. 6 shows the importance of the top 40 variables in the MLA prediction obtained from the random forest regression model.
 233 The importance of these 40 variables accounts for 78% of the total importance among all 76 variables. Spectral features
 234 account for 30% of the importance, which is higher than that of other features. Among the spectral features, NDVI, near-
 235 infrared (NIR) band, and red band reflectance are most critical for MLA prediction. The importance of BRDF features is
 236 comparable to that of climatic variables (21% vs. 20%), followed by terrain features (7%). Among the BRDF features, the
 237 NIR BRDF information shows a higher contribution than the red band, with importance in the following order: geometrically
 238 scattered kernel > isotropic scattering kernel > volumetric scattering kernel. The importance ranking of the climatic variables
 239 follows the order of precipitation \approx solar radiation > temperature. Additionally, elevation shows a considerable impact on the
 240 MLA prediction.



241
 242 **Figure 6.** The importance of variables in the mean leaf inclination angle prediction. NIR, Red, Green, and Blue denote the nadir
 243 reflectance in near-infrared, red, green, and blue bands, respectively; geo, iso, and vol represent kernel coefficients of geometric-optical
 244 surface scattering, isotropic scattering, and volumetric scattering, respectively. The suffixes p $\times\times$, mean, and std represent $\times\times\%$ quantile,
 245 mean, and standard deviation, respectively.



246 Fig. 7 illustrates the relationships between the upscaled MLA samples and the 16 most important variables. Overall, MLA
247 decreases with the increase of NDVI, NIR reflectance, and NIR BRDF kernel parameters, whereas it increases with the
248 standard deviation of NDVI. MLA is negatively correlated with solar radiation, precipitation, and temperature. Additionally,
249 MLA increases with increasing the standard deviation of solar radiation (corresponding to mid-to-high latitude regions),
250 while it decreases with the increase in the standard deviation of precipitation (corresponding to tropical and subtropical
251 regions with high precipitation). MLA increases slightly with elevation.



252

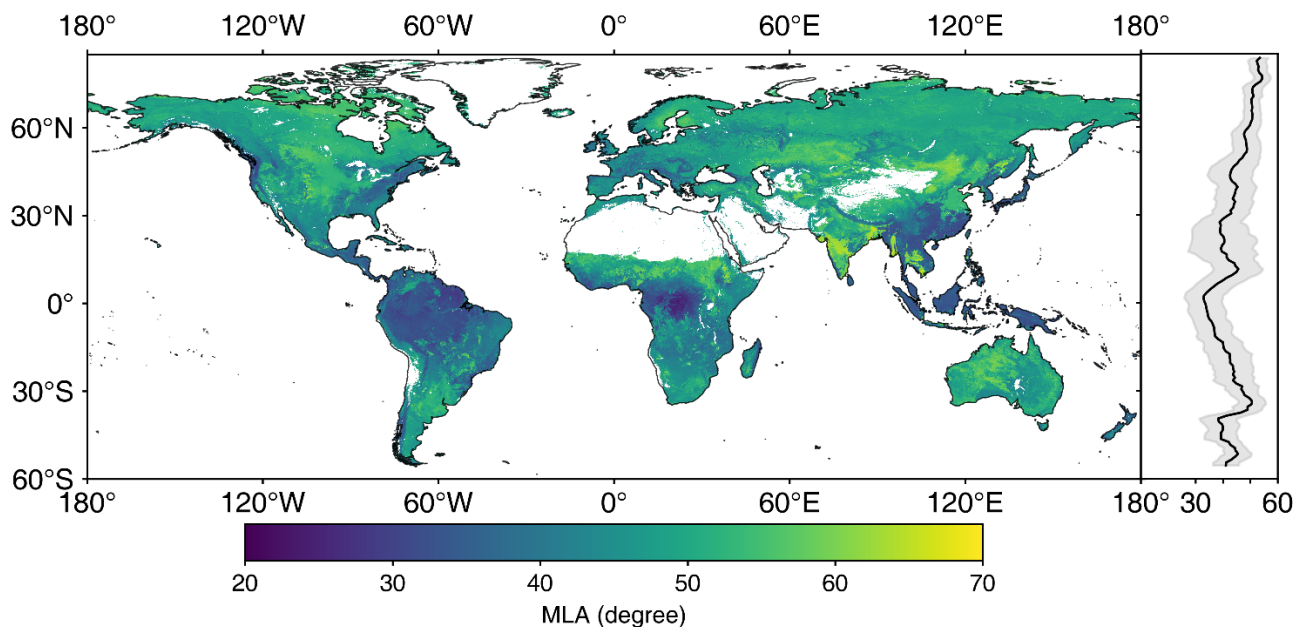
253 **Figure 7.** Relationships between mean leaf inclination angle (MLA) and different predictive variables. See Fig. 6 for different variables.

254 3.3 Global MLA and G(0) maps

255 Fig. 8 shows the spatial distribution of the global 500 m MLA product. Central Asia (grasslands), southern India (cereal
256 crops), and the central United States (grasslands and cereal crops) show higher MLAs of approximately 60°, whereas the
257 rainforests and Southeast Asia forests have more horizontal leaves with MLAs of around 30° (Fig. 8 and S2). MLA increases
258 with latitude, from $32.93 \pm 7.03^\circ$ around the equator ($\sim 1.5^\circ$ N) to $53.48 \pm 3.20^\circ$ in the northern tundra ($\sim 76.5^\circ$ N). Variation
259 in MLA decreases as latitude increases (Fig. 8). Among different PFTs, cereal crops show the highest MLA ($54.65 \pm 6.28^\circ$),



260 while evergreen broadleaf forest has the lowest MLA ($34.40 \pm 6.42^\circ$), and PFTs follow the order: CRO-C > CRO-B > DNF >
 261 SHR > ENF \approx GRA > DBF > EBF (Table 4). Grassland, broadleaf forest, and evergreen needleleaf forests show larger MLA
 262 variations than other PFTs, whereas deciduous needleleaf forests show minimal variation. The global vegetation MLA is
 263 41.47° , with a standard deviation of 9.55° , which is comparable to the MLA of DBF ($41.23 \pm 6.58^\circ$) (Fig. 9a and Table 4).

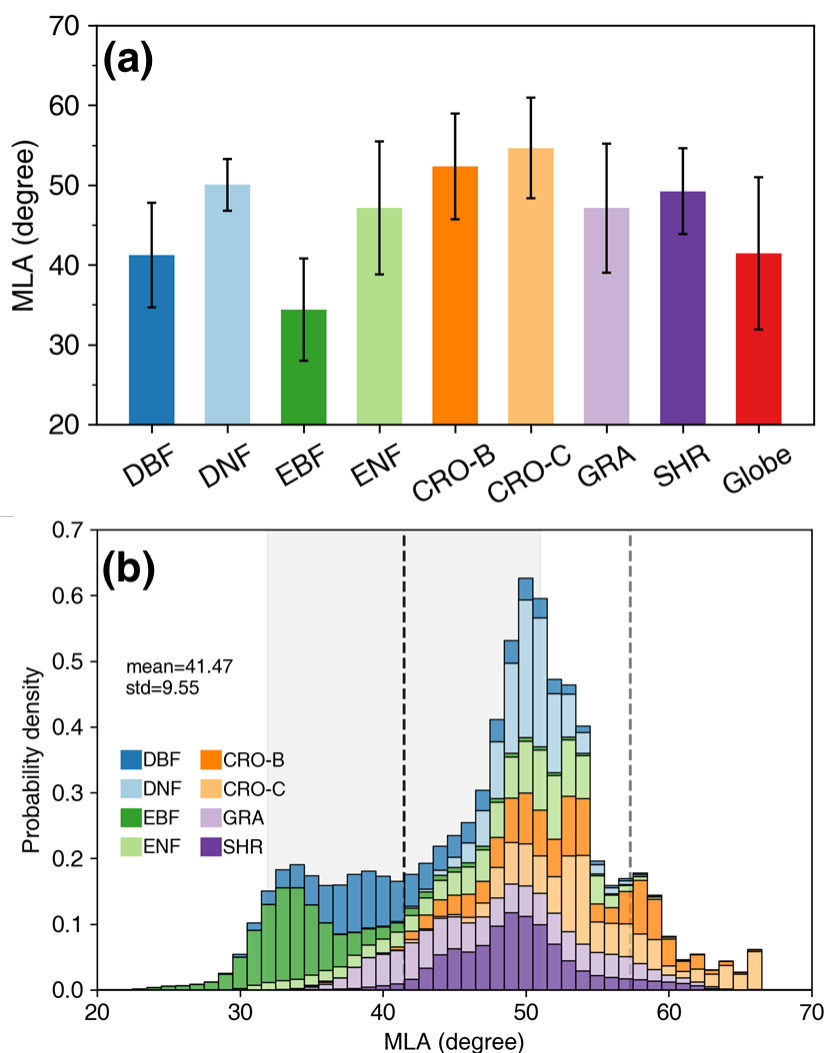


264
 265 **Figure 8.** The global mean leaf inclination angle (MLA) map. The right panel shows the MLA latitudinal mean (solid line) and the
 266 standard deviation values (shaded area) weighted by leaf area index.

267 **Table 4.** Statistics of global mean leaf inclination angle (MLA), nadir leaf projection function ($G(0)$), and inclination index (χ_L) for
 268 different plant functional types (PFT). STD is the standard deviation. The χ_L is converted from MLA ($\chi_L = 2\cos(\text{MLA}) - 1$) (Lawrence
 269 [et al., 2019](#)).

PFT	DBF	DNF	EBF	ENF	CRO-B	CRO-C	GRA	SHR	Globe
Area proportion(%)	14.02	6.32	15.08	11.42	2.99	6.84	28.45	14.88	100.00
MLA($^\circ$)	41.23	50.05	34.40	47.13	52.35	54.65	47.12	49.23	41.47
STD of MLA ($^\circ$)	6.58	3.24	6.42	8.35	6.63	6.28	8.08	5.35	9.55
$G(0)$	0.69	0.58	0.76	0.61	0.55	0.52	0.61	0.59	0.68
STD of $G(0)$	0.07	0.03	0.06	0.08	0.07	0.08	0.09	0.06	0.11
χ_L	0.50	0.28	0.65	0.36	0.22	0.16	0.36	0.31	0.50

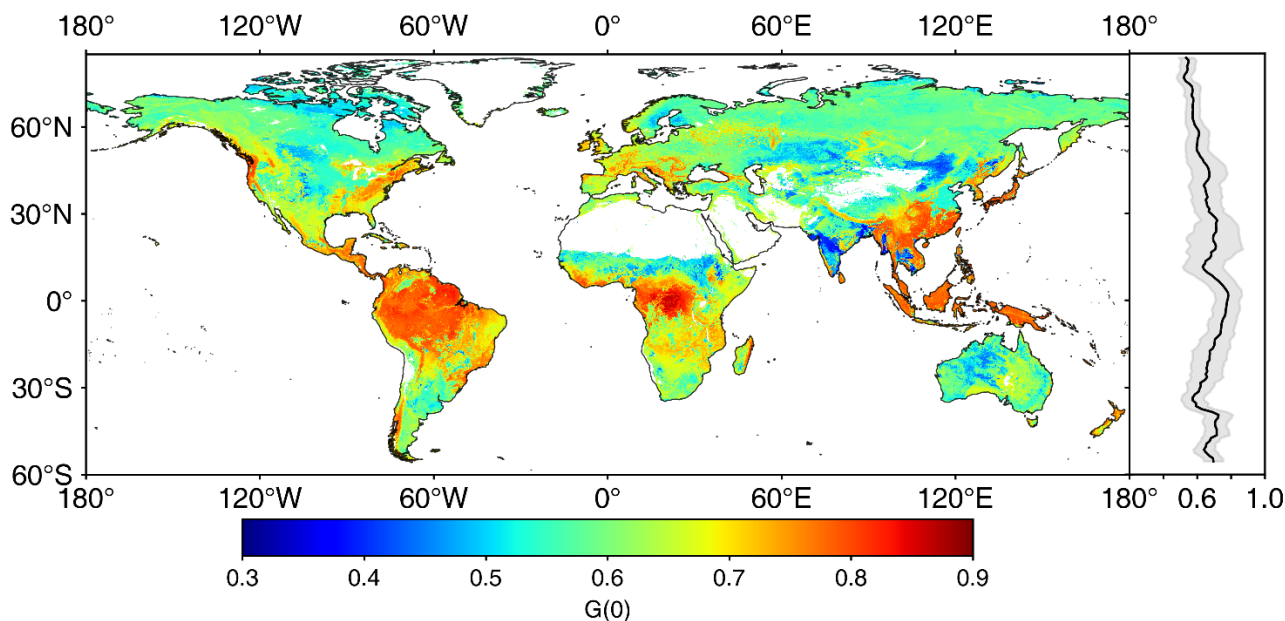
270
 271 The global MLA exhibits an asymmetric probability density distribution toward the lower MLA (Fig. 9b). It roughly
 272 presents three peaks, with the highest peak ($\sim 51^\circ$) containing DNF, ENF, CRO, GRA, and SHR. The moderate peak ($\sim 35^\circ$)
 273 is mainly composed of EBF and DBF, while the third peak ($\sim 58^\circ$) is dominated by crops. The MLAs of crops and some
 274 grasslands are close to the MLA of the spherical distribution (57.30°). The global MLA (41.47°) is 15.83° (38%) smaller
 275 than the MLA of the spherical distribution because the vegetation MLA is mostly less than 57.30° (Fig. 9b).



276

277 **Figure 9.** Statistics (a) and probability density distributions (b) of the global mean leaf inclination angle (MLA) for different plant
278 functional types. The error bars in (a) represent the standard deviation. The black dash line and shade area in (b) indicate the global MLA
279 mean and standard deviation. The gray dashed line represents the MLA ($=57.30^\circ$) of spherical leaf angle distribution. The mean, standard
280 deviation, and probability density values are weighted by leaf area index. See Fig. 1 for the acronyms.

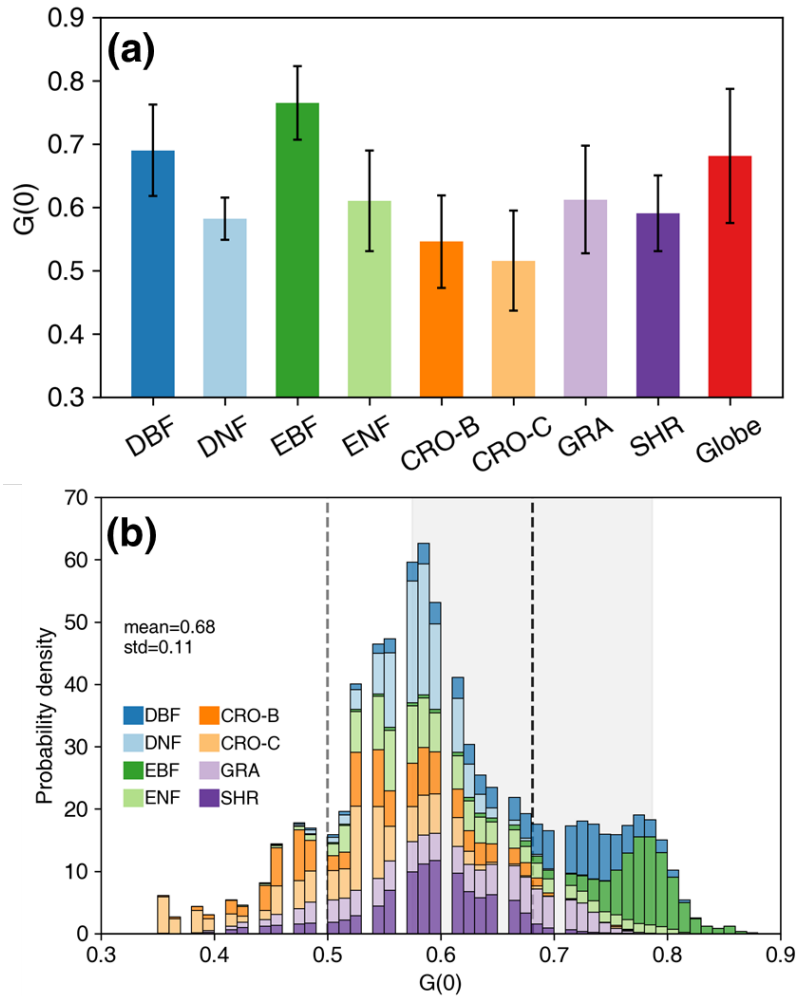
281 Fig. 10 displays the spatial distribution of global $G(0)$ generated from MLA. Overall, the global $G(0)$ shows an opposite
282 pattern with the global MLA. The $G(0)$ values in Central Asia (grasslands, Fig. S2), southern India (cereal crops), and the
283 central United States (grasslands and cereal crops) are relatively lower than those in tropical rainforests, forests in Southeast
284 Asia, and forests in the eastern United States. $G(0)$ generally decreases slowly with latitude, from 0.78 ± 0.08 at the equator
285 ($\sim 1.5^\circ$ N) to 0.52 ± 0.04 in the northern tundra ($\sim 76.5^\circ$ N).



286

287 **Figure 10.** The global nadir leaf projection function ($G(0)$) map. The right panel shows the $G(0)$ mean (solid line) and standard deviation
288 values (shaded area) weighted by leaf area index.

289 Among different PFTs, EBF has the highest $G(0)$, at approximately 0.76 ± 0.06 (Fig. 11a, Table 4), whereas cereal crops
290 show the lowest value, at approximately 0.52 ± 0.08 . The DBF $G(0)$ is comparable to the global average. The $G(0)$ of broad-
291 leaved forests is greater than that of other PFTs (Fig. 11a, Table 4). The global $G(0)$ probability density distribution peaks at
292 0.52–0.65, with an asymmetric distribution (Fig. 11b). The proportion on the right side of the peak is larger than that on the
293 left. The peak of the global $G(0)$ distribution mainly contains DNF, ENF, CRO, GRA, and SHR. The left side of the peak is
294 mainly composed of crops, while the right side is dominated by broad-leaved forests and some shrubs. The spherical
295 distribution $G(0)$ (0.50) is mainly represented by crops and a small amount of grassland, where $G(0)$ also shows a large
296 variation (~ 0.35). The spherical distribution $G(0)$ is 0.18 (26%) less than the global average $G(0)$ (0.68), as most vegetation
297 $G(0)$ is greater than 0.50 (Fig. 11b).

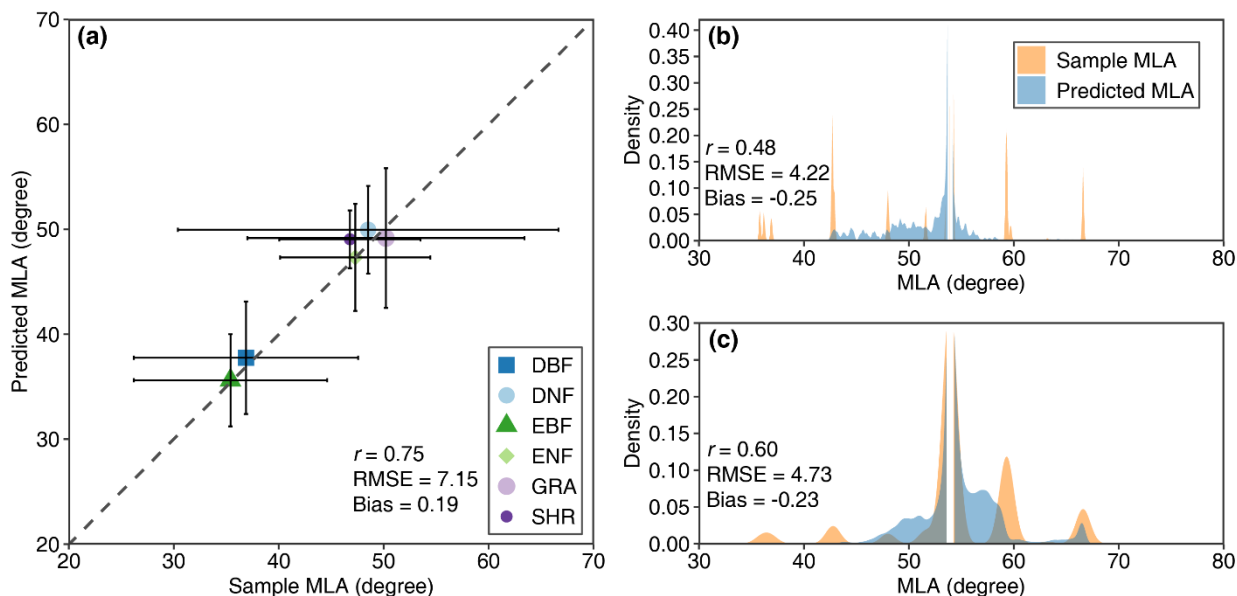


298

299 **Figure 11.** Statistics (a) and probability density distributions (b) of the global nadir leaf projection function ($G(0)$) for different plant
 300 functional types. The error bars in (a) represent the standard deviation. The black dash line and shade area in (b) indicate the global $G(0)$
 301 mean and standard deviation. The gray dashed line represents the $G(0)$ ($=0.50$) of spherical leaf angle distribution. The mean, standard
 302 deviation, and probability density values are weighted by leaf area index. See Fig. 1 for the acronyms.

303 3.4 Evaluation of global MLA

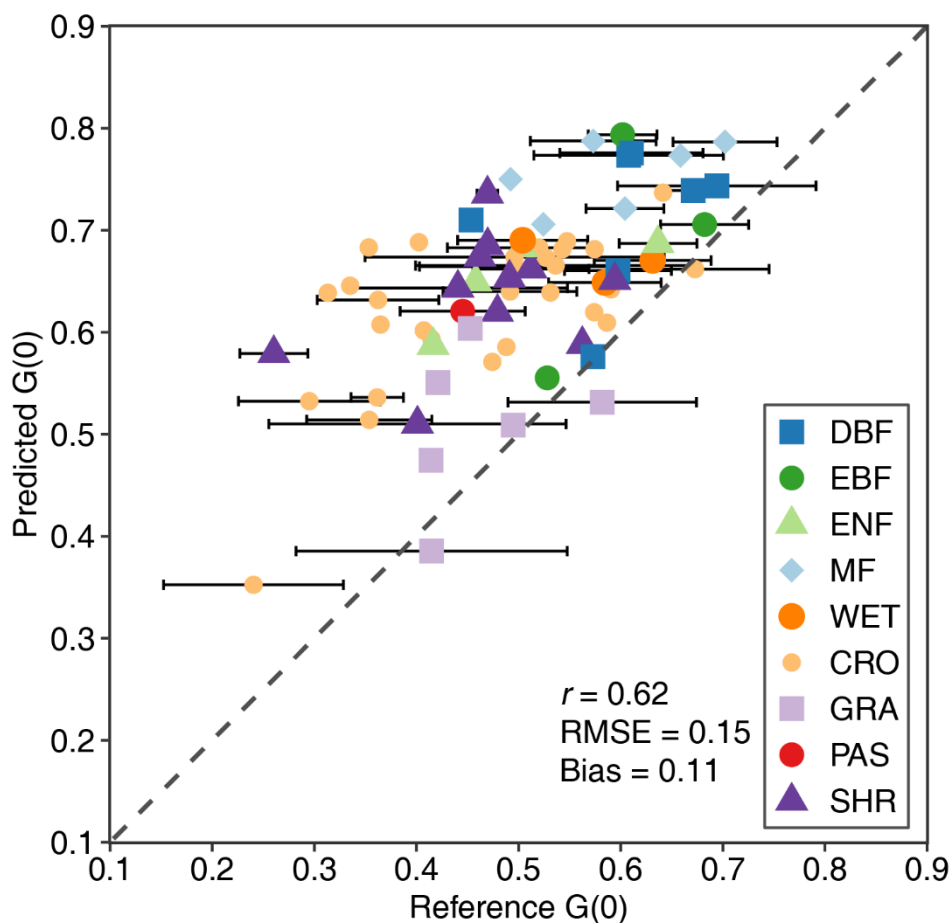
304 Fig. 12 shows the comparison between the predicted MLA and upscaled MLA samples using the ten-fold cross-validation
 305 method. For noncrops, the predicted MLA is moderately consistent with the upscaled sample MLA ($r = 0.75$, $\text{RMSE} =$
 306 7.15°), with 83% of samples having residuals $< 10^\circ$ and 94% of samples having residuals $< 15^\circ$. For DNF and SHR, the
 307 predicted MLA compresses the variation range of sample MLA (Fig. 12a). For crops, the predicted MLA of CRO-C shows
 308 higher consistency ($r = 0.60$) than that of CRO-B ($r = 0.48$). (Fig. 12b and c).



309

310 **Figure 12.** Comparisons between predicted MLA and sample MLA for noncrop (a), broadleaf crops (b), and cereal crops (c) (See Fig. 1
311 for the acronyms). The error bar in (a) represents the standard deviation.

312 Fig. 13 compares $G(0)$ derived from the MLA and high-resolution reference data. The MLA-derived $G(0)$ shows moderate
313 consistency with the reference $G(0)$ ($r = 0.62$), and 65% of the estimated $G(0)$ residuals are < 0.15 , and 84% of the residuals
314 are < 0.20 . The estimated $G(0)$ generally overestimates (bias = 0.11), especially when $G(0)$ is low (< 0.60), mainly for crops,
315 pasture, woody wetlands, and shrubs, whereas grasslands show better consistency. The estimated $G(0)$ is temporally more
316 stable than the reference $G(0)$ which is generally greater than 0.50 and displays seasonal variation (horizontally distributed
317 bars in Fig. 13).



318

319 **Figure 13.** Comparisons of $G(0)$ derived from mean leaf inclination angle and high-resolution reference data for different plant functional
320 types (see Fig. 2 for the acronyms). The error bar represents the standard deviation of reference $G(0)$ at different seasons.

321 4 Discussion

322 4.1 Global MLA and $G(0)$

323 This study compiled global LIA field measurements and generated the first global 500 m MLA and $G(0)$ maps (Figs. 8 and
324 10). These maps show the average MLA and $G(0)$ conditions during the growing seasons from 2001 to 2022. Overall, the
325 global MLA is lowest around the equator and increases with latitude (Figs. 8 and 10). This accords with the MLA latitude
326 variation derived from model simulations (Huemmrich, 2013). Crops have higher MLA than broadleaf forests whose leaves
327 are relatively horizontal. The global MLA and $G(0)$ maps enhance our understanding of the global distribution of MLA and
328 $G(0)$ and should be useful in radiative transfer modeling, remote sensing of vegetation parameters, land surface modeling,
329 and ecological studies.



330 The globally derived MLA is 41.47° , which is consistent with the LIA measurements (40.74° , Tables 3 and 4). However, the
331 derived MLAs of DBF, DNF, CRO-B, and SHR are approximately 10° greater than the measured MLAs. It is noted that the
332 number and spatial distribution of LIA measurements for these biomes are limited. For example, the global CRO-B areas are
333 dominated by soybeans with higher LIA (Table S2), and the LIA measurements for soybeans are limited, which caused the
334 CRO-B MLA in the global map to be greater than that in the measurement statistics (Tables 3 and 4). The poor crop MLA
335 prediction (Fig. 12b) is mainly caused by a small number of samples and the strong seasonal variation. It is difficult to
336 consider within-crop LIA variation when typical MLA values are assigned to different crops.

337 The global MLA was evaluated through a comparison of the MLA-derived $G(0)$ with the high-resolution reference (Fig. 13).
338 The result shows that MLA-derived $G(0)$ overestimates at low values, especially for CRO, PAS, SHR, and WET. The
339 overestimation is caused by the underestimation of MLA at high values (Fig. 12), vegetation structural complexity, and
340 seasonal variation (Fig. 13). In addition, the overestimation can be explained by the CI angular effect and the inability to
341 distinguish branches and leaves in the generating high-resolution $G(0)$. Previous studies illustrated CI increases with the
342 view zenith angle (Fang, 2021), which causes whole $CI > CI(0)$ and thus leads to the underestimation of reference $G(0)$ (Eq.
343 (6) and (7)). The inability to distinguish branches and leaves results in the underestimation of reference $G(0)$ due to the
344 higher inclination angle of the trunk (Liu et al., 2019). Compared with the previous $G(0)$ derived from global vegetation
345 biophysical products (Eq. (7)) ($R^2 = 0.11$, $RMSE = 0.53$) (Li et al., 2022), the MLA-derived $G(0)$ performs better ($R^2 = 0.38$,
346 $RMSE = 0.15$). In addition, $G(\theta)$ in any direction can be derived from the global MLA (Eq. (3)). Since $G(\theta)$ varies most
347 significantly in the nadir direction for different MLA (Wilson, 1959), the uncertainty of $G(\theta)$ derived from the global MLA
348 in other directions will be smaller than that of $G(0)$.

349 4.2 The relationship between MLA and other variables

350 Analysis of the relationships between MLA and other features in the MLA mapping process reveals that MLA is negatively
351 correlated with NDVI, NIR reflectance, and NIR BRDF kernel coefficients (Fig. 7). These findings are consistent with other
352 simulation and experimental studies (Zou and Möttus, 2015; Liu et al., 2012; Dong et al., 2019; Jacquemoud et al., 1994). A
353 higher MLA canopy is characterized by a lower interception capability, which increases NIR downward radiation and
354 reduces the NIR multiple scattering within the canopy and the canopy reflectance (Liu et al., 2012). This results in negative
355 correlations between MLA and NIR reflectance and vegetation index. The negative relationships between MLA and
356 radiation, precipitation, and temperature (Fig. 7) are related to the vegetation adaptation mechanism. Under suitable climate
357 conditions, horizontal leaves can enhance light interception and increase the photosynthesis rate (Van Zanten et al., 2010;
358 King, 1997). The positive correlation between MLA and the standard deviation of radiation and temperature (Fig. 7)
359 indicates that the MLA is more vertical in areas with significant seasonal changes in radiation and temperature (mid to high-
360 latitude areas) because vertical leaves maximize intercepted radiation under low solar altitudes at mid to high-latitude areas
361 (Huemmrich, 2013).



362 4.3 Use of the new MLA map

363 The spherical LAD assumption has been widely adopted in the literature ([Tang et al., 2016](#); [Zhao et al., 2020](#); [Wang and](#)
364 [Fang, 2020](#)). This study demonstrates that the spherical assumption is valid only for cereal crops, but not for broadleaf
365 forests (Tables 3 and 4). This finding is consistent with previous local LIA measurements ([De Wit, 1965](#); [Pisek et al., 2013](#);
366 [Yan et al., 2021](#)). For crops, the spherical assumption may even become invalid because of seasonality and species diversity
367 (Table S2, Figs. 5 and 9). Fig. 13 shows that most of the reference $G(0)$ values are greater than 0.50, while the spherical
368 distribution would underestimate the interception of radiation and rainfall (Figs. 9 and 11) ([Stadt and Loeffers, 2000](#)). In
369 current LSMs, a constant LIA is commonly assigned for each PFT ([Majasalmi and Bright, 2019](#)). For example, the
370 Community Land Model V5 (CLM5) (Table S4) ([Lawrence et al., 2019](#)) uses lower inclination indices and higher LIA
371 values than our results (Tables 3 and 4) and thus may underestimate canopy interception. The global LIA map generated in
372 this study provides a more reasonable LIA parameterization strategy for the application communities.

373 4.4 Limitations and prospects

374 The limitations of this study relate to the small number of LIA measurements, especially continuous measurements. First,
375 within-species LIA variations were neglected in the spatial expansion due to limited spatial coverage of existing LIA-
376 measured data (Section 2.3.1). This may introduce some errors, especially for crops. Second, the LIA measurement data
377 were obtained using different sampling schemes and methods. This inconsistency may influence the results. Third, for
378 forests, the contribution of the understory was not considered. Typically, the understory is characterized by more horizontal
379 leaves, and ignoring the understory may lead to an MLA overestimation ([Utsugi et al., 2006](#)). Nevertheless, a previous study
380 showed that the relative contribution of the understory to the overall MLA is less than 10% ([Li et al., 2022](#)). Finally, only the
381 growing season MLA was calculated, whereas the seasonal and long-term variations of MLA were not considered due to the
382 lack of continuous LIA measurements.

383 In the future, more efficient LIA observation systems should be developed to provide continuous LIA data ([Kattenborn et al.,](#)
384 [2022](#)). LIA measurements can be integrated into existing ground observation networks, such as the National Ecological
385 Observatory Network (NEON) ([Kao et al., 2012](#)), Integrated Carbon Observation System (ICOS) ([Gielen et al., 2018](#)), and
386 Terrestrial Ecosystem Research Network (TERN) ([Karan et al., 2016](#)), to enhance temporal LIA measurements in larger
387 spatial extent, especially for DNF and crops. The formulation of standard measurement and data-sharing protocols will
388 promote data-sharing and utilization ([Li et al., 2023](#)). Multiangle reflectance ([Jacquemoud et al., 2009](#); [Goel and Thompson,](#)
389 [1984](#); [Jacquemoud et al., 1994](#)) or light detection and ranging ([Zheng and Moskal, 2012](#); [Bailey and Mahaffee, 2017](#); [Itakura](#)
390 [and Hosoi, 2019](#)) are encouraging remote sensing tools that can help to derive temporally continuous and high-resolution
391 MLA data.



392 **5 Conclusion**

393 This study compiled existing global LIA measurements and generated the first global 500 m MLA and G(0) products by
394 gap-filling the LIA measurement data using a random forest regressor. The mean of global LIA measurements is 40.74° and
395 cereal crops show the highest MLA (59.11°). The global MLA shows an explicit spatial distribution and the value increases
396 with latitude. The global MLA is $41.47^\circ \pm 9.55^\circ$ and follows the order of CRO-C > CRO-B > DNF > SHR > ENF \approx GRA >
397 DBF > EBF. The predicted MLA presents a medium consistency ($r = 0.75$, RMSE = 7.15°) with the validation samples for
398 noncrops. For crops, the results are relatively poorer ($r = 0.48$ and 0.60 for broadleaf crops and cereal crops) because of
399 limited LIA measurements and strong seasonality. The G(0) derived from MLA is moderately consistent with the reference
400 G(0) ($r = 0.62$).

401 The MLA and G(0) products obtained in this study would enhance our understanding of global LIA and assist remote
402 sensing retrieval and land surface modeling studies. These products provide a more realistic parameterization strategy than
403 the commonly used spherical LAD and PFT-specific MLA assignment. Note the global MLA and G(0) products mainly
404 represent the typical state during the growing season. These products can be further improved and temporal MLA data can
405 be obtained through continuous measurements and remote sensing retrieval.

406 **Data availability**

407 The global MLA and G(0) products are available in: Li, S. and Fang, H. 2024, <https://doi.org/10.5281/zenodo.10940673>. (Li
408 and Fang, 2024). The related code can be accessed at https://code.earthengine.google.com/?accept_repo=users/SiJia/MTA.

409 **Author contributions**

410 HF and SL conceptualized this work. SL compiled global LIA measurements, generated global products, and curated the
411 datasets. SL and HF wrote the manuscript. HF was responsible for funding.

412 **Competing interests**

413 The contact author has declared that none of the authors has any competing interests.

414 **Acknowledgements**

415 The authors are grateful to TRY and many other researchers for sharing the LIA measurement data. Jens Kattge at the Max
416 Planck Institute for Biogeochemistry and Dongliang Cheng at Fujian Normal University provided the TRY species location
417 data and LIA measurements in China's subtropical regions, respectively.



418

419 **Financial support**

420 This work was mainly supported by the National Natural Science Foundation of China (42171358).

421 **References**

422 Bailey, B. N. and Mahaffee, W. F.: Rapid measurement of the three-dimensional distribution of leaf orientation and the leaf
423 angle probability density function using terrestrial LiDAR scanning, *Remote Sens. Environ.*, 194, 63-76,
424 10.1016/j.rse.2017.03.011, 2017.

425 Bayat, B., van der Tol, C., and Verhoef, W.: Integrating satellite optical and thermal infrared observations for improving
426 daily ecosystem functioning estimations during a drought episode, *Remote Sens. Environ.*, 209, 375-394,
427 10.1016/j.rse.2018.02.027, 2018.

428 Boryan, C., Yang, Z., Mueller, R., and Craig, M.: Monitoring US agriculture: the US department of agriculture, national
429 agricultural statistics service, cropland data layer program, *Geocarto International*, 26, 341-358, 2011.

430 Brown, L. A., Meier, C., Morris, H., Pastor-Guzman, J., Bai, G., Lerebourg, C., Gobron, N., Lanconelli, C., Clerici, M., and
431 Dash, J.: Evaluation of global leaf area index and fraction of absorbed photosynthetically active radiation products over
432 North America using Copernicus Ground Based Observations for Validation data, *Remote Sens. Environ.*, 247,
433 10.1016/j.rse.2020.111935, 2020.

434 Campbell, G.: Derivation of an angle density function for canopies with ellipsoidal leaf angle distributions, *Agricultural and
435 forest meteorology*, 49, 173-176, 1990.

436 Chen, J. M., Ju, W., Ciais, P., Viovy, N., Liu, R., Liu, Y., and Lu, X.: Vegetation structural change since 1981 significantly
437 enhanced the terrestrial carbon sink, *Nat Commun*, 10, 4259, 10.1038/s41467-019-12257-8, 2019.

438 Chen, X., Zhong, Q.-L., Lyu, M., Wang, M., Hu, D., Sun, J., and Cheng, D.: Trade-off relationship between light
439 interception and leaf water shedding at different canopy positions of 73 broad-leaved trees of Yangji Mountain in Jiangxi
440 Province, China, *SCIENTIA SINICA Vitae*, 51, 91-101, 10.1360/SSV-2020-0218, 2021.

441 Chianucci, F., Pisek, J., Raabe, K., Marchino, L., Ferrara, C., and Corona, P.: A dataset of leaf inclination angles for
442 temperate and boreal broadleaf woody species, *Annals of Forest Science*, 75, 50-50, 10.1007/s13595-018-0730-x, 2018.

443 Crawford, C. J., Roy, D. P., Arab, S., Barnes, C., Vermote, E., Hulley, G., Gerace, A., Choate, M., Engebretson, C.,
444 Micijevic, E., Schmidt, G., Anderson, C., Anderson, M., Bouchard, M., Cook, B., Dittmeier, R., Howard, D., Jenkerson, C.,
445 Kim, M., Kleyians, T., Maiersperger, T., Mueller, C., Neigh, C., Owen, L., Page, B., Pahlevan, N., Rengarajan, R., Roger, J.-
446 C., Sayler, K., Scaramuzza, P., Skakun, S., Yan, L., Zhang, H. K., Zhu, Z., and Zahn, S.: The 50-year Landsat collection 2
447 archive, *Science of Remote Sensing*, 8, 100103, <https://doi.org/10.1016/j.srs.2023.100103>, 2023.



- 448 d'Andrimont, R., Verhegghen, A., Lemoine, G., Kempeneers, P., Meroni, M., and van der Velde, M.: From parcel to
449 continental scale – A first European crop type map based on Sentinel-1 and LUCAS Copernicus in-situ observations,
450 Remote Sens. Environ., 266, 112708, <https://doi.org/10.1016/j.rse.2021.112708>, 2021.
- 451 de Wit, C. T.: Photosynthesis of leaf canopies, Pudoc, 1965.
- 452 Dong, J., fu, y., wang, j., Tian, H., Fu, S., Niu, Z., Han, W., Zheng, Y., Huang, J., and Yuan, W.: 30m winter wheat
453 distribution map of China for four years (2016-2019), 10.6084/m9.figshare.12003990.v2, 2020.
- 454 Dong, T., Liu, J., Shang, J., Qian, B., Ma, B., Kovacs, J. M., Walters, D., Jiao, X., Geng, X., and Shi, Y.: Assessment of red-
455 edge vegetation indices for crop leaf area index estimation, Remote Sens. Environ., 222, 133-143, 10.1016/j.rse.2018.12.032,
456 2019.
- 457 Fang, H.: Canopy clumping index (CI): A review of methods, characteristics, and applications, Agricultural and Forest
458 Meteorology, 303, 108374, <https://doi.org/10.1016/j.agrformet.2021.108374>, 2021.
- 459 Fang, H., Li, S., Zhang, Y., Wei, S., and Wang, Y.: New insights of global vegetation structural properties through an
460 analysis of canopy clumping index, fractional vegetation cover, and leaf area index, Science of Remote Sensing, 100027,
461 <https://doi.org/10.1016/j.srs.2021.100027>, 2021.
- 462 Fisette, T., Rollin, P., Aly, Z., Campbell, L., Daneshfar, B., Filyer, P., Smith, A., Davidson, A., Shang, J., and Jarvis, I.:
463 AAFC annual crop inventory, 2013 Second International Conference on Agro-Geoinformatics (Agro-Geoinformatics), 270-
464 274,
- 465 Foley, J. A., Prentice, I. C., Ramankutty, N., Levis, S., Pollard, D., Sitch, S., and Haxeltine, A.: An integrated biosphere
466 model of land surface processes, terrestrial carbon balance, and vegetation dynamics, Global biogeochemical cycles, 10,
467 603-628, 1996.
- 468 Gielen, B., Acosta, M., Altimir, N., Buchmann, N., Cescatti, A., Ceschia, E., Fleck, S., Hörtnagl, L., Klumpp, K., Kolari, P.,
469 Lohila, A., Loustau, D., Marañón-Jimenez, S., Manise, T., Matteucci, G., Merbold, L., Metzger, C., Moureaux, C.,
470 Montagnani, L., Nilsson, M. B., Osborne, B., Papale, D., Pavelka, M., Saunders, M., Simioni, G., Soudani, K., Sonntag,
471 O., Tallec, T., Tuittila, E.-S., Peichl, M., Pokorny, R., Vincke, C., and Wohlfahrt, G.: Ancillary vegetation measurements at
472 ICOS ecosystem stations, International Agrophysics, 32, 645-664, 10.1515/intag-2017-0048, 2018.
- 473 Goel, N. S. and Thompson, R. L.: Inversion of vegetation canopy reflectance models for estimating agronomic variables. V.
474 Estimation of leaf area index and average leaf angle using measured canopy reflectances, Remote Sens. Environ., 16, 69-85,
475 10.1016/0034-4257(84)90028-2, 1984.
- 476 Han, J., Zhang, Z., Luo, Y., Cao, J., Zhang, L., Cheng, F., Zhuang, H., Zhang, J., and Tao, F.: NESEA-Rice10: high-
477 resolution annual paddy rice maps for Northeast and Southeast Asia from 2017 to 2019, Earth System Science Data, 13,
478 5969-5986, 10.5194/essd-13-5969-2021, 2021.
- 479 Hinojo-Hinojo, C. and Goulden, M.: A compilation of canopy leaf inclination angle measurements across plant species and
480 biome types, 10.7280/D1T97H, 2020.



- 481 Huemmrich, K. F.: Simulations of Seasonal and Latitudinal Variations in Leaf Inclination Angle Distribution: Implications
482 for Remote Sensing, *Advances in Remote Sensing*, 02, 93-101, 10.4236/ars.2013.22013, 2013.
- 483 Itakura, K. and Hosoi, F.: Estimation of Leaf Inclination Angle in Three-Dimensional Plant Images Obtained from Lidar,
484 *Remote Sensing*, 11, 10.3390/rs11030344, 2019.
- 485 Jacquemoud, S., Flasse, S., Verdebout, J., and Schmuck, G.: Comparison of Several Optimization Methods To Extract
486 Canopy Biophysical Parameters - Application To Caesar Data, 291-298, 1994.
- 487 Jacquemoud, S., Verhoef, W., Baret, F., Bacour, C., Zarco-Tejada, P. J., Asner, G. P., François, C., and Ustin, S. L.:
488 PROSPECT+SAIL models: A review of use for vegetation characterization, *Remote Sens. Environ.*, 113, S56-S66,
489 10.1016/j.rse.2008.01.026, 2009.
- 490 Kao, R. H., Gibson, C. M., Gallery, R. E., Meier, C. L., Barnett, D. T., Docherty, K. M., Blevins, K. K., Travers, P. D.,
491 Azuaje, E., Springer, Y. P., Thibault, K. M., McKenzie, V. J., Keller, M., Alves, L. F., Hinckley, E.-L. S., Parnell, J., and
492 Schimel, D.: NEON terrestrial field observations: designing continental-scale, standardized sampling, *Ecosphere*, 3, art115,
493 10.1890/es12-00196.1, 2012.
- 494 Karan, M., Liddell, M., Prober, S. M., Arndt, S., Beringer, J., Boer, M., Cleverly, J., Eamus, D., Grace, P., Van Gorsel, E.,
495 Hero, J. M., Hutley, L., Macfarlane, C., Metcalfe, D., Meyer, W., Pendall, E., Sebastian, A., and Wardlaw, T.: The
496 Australian SuperSite Network: A continental, long-term terrestrial ecosystem observatory, *Sci. Total Environ.*, 568, 1263-
497 1274, 10.1016/j.scitotenv.2016.05.170, 2016.
- 498 Kattenborn, T., Richter, R., Guimarães-Steinicke, C., Feilhauer, H., and Wirth, C.: AngleCam: Predicting the temporal
499 variation of leaf angle distributions from image series with deep learning, *Methods in Ecology and Evolution*, 13, 2531-2545,
500 10.1111/2041-210x.13968, 2022.
- 501 Kattge, J., Bonisch, G., Diaz, S., Lavorel, S., and Prentice, I. C.: TRY plant trait database - enhanced coverage and open
502 access, *Glob Chang Biol*, 26, 119-188, 10.1111/gcb.14904, 2020.
- 503 King, D. A.: The Functional Significance of Leaf Angle in Eucalyptus, *Aust. J. Bot.*, 45, 619-639,
504 <https://doi.org/10.1071/BT96063>, 1997.
- 505 Lang, A. R. G.: Leaf orientation of a cotton plant, *Agricultural Meteorology*, 11, 37-51, 10.1016/0002-1571(73)90049-6,
506 1973.
- 507 Lawrence, D. M., Fisher, R. A., Koven, C. D., Oleson, K. W., Swenson, S. C., Bonan, G., Collier, N., Ghimire, B., Van
508 Kampenhout, L., and Kennedy, D.: The Community Land Model version 5: Description of new features, benchmarking, and
509 impact of forcing uncertainty, *Journal of Advances in Modeling Earth Systems*, 11, 4245-4287, 2019.
- 510 Li, S. and Fang, H.: Global Leaf Inclination Angle (LIA) and Nadir Leaf Projection Function (G(0)) Products, Zenodo
511 [dataset], 10.5281/zenodo.10940673, 2024.
- 512 Li, S., Fang, H., and Zhang, Y.: Determination of the Leaf Inclination Angle (LIA) through Field and Remote Sensing
513 Methods: Current Status and Future Prospects, *Remote Sensing*, 15, 946, 2023.



- 514 Li, S., Fang, H., Zhang, Y., and Wang, Y.: Comprehensive evaluation of global CI, FVC, and LAI products and their
515 relationships using high-resolution reference data, *Science of Remote Sensing*, 6, 10.1016/j.srs.2022.100066, 2022.
- 516 Liu, J., Pattey, E., and Jégo, G.: Assessment of vegetation indices for regional crop green LAI estimation from Landsat
517 images over multiple growing seasons, *Remote Sens. Environ.*, 123, 347-358, 10.1016/j.rse.2012.04.002, 2012.
- 518 Liu, J., Wang, T., Skidmore, A. K., Jones, S., Heurich, M., Beudert, B., and Premier, J.: Comparison of terrestrial LiDAR
519 and digital hemispherical photography for estimating leaf angle distribution in European broadleaf beech forests, *ISPRS
520 Journal of Photogrammetry and Remote Sensing*, 158, 76-89, 10.1016/j.isprsjprs.2019.09.015, 2019.
- 521 Maes, W. and Steppe, K.: Estimating evapotranspiration and drought stress with ground-based thermal remote sensing in
522 agriculture: a review, *J. Exp. Bot.*, 63, 4671-4712, 2012.
- 523 Majasalmi, T. and Bright, R. M.: Evaluation of leaf-level optical properties employed in land surface models – example with
524 CLM 5.0, *Geoscientific Model Development Discussions*, 1-24, 2019.
- 525 Mantilla-Perez, M. B. and Salas Fernandez, M. G.: Differential manipulation of leaf angle throughout the canopy: current
526 status and prospects, *J. Exp. Bot.*, 68, 5699-5717, 2017.
- 527 Muñoz-Sabater, J., Dutra, E., Agustí-Panareda, A., Albergel, C., Arduini, G., Balsamo, G., Boussetta, S., Choulga, M.,
528 Harrigan, S., Hersbach, H., Martens, B., Miralles, D. G., Piles, M., Rodríguez-Fernández, N. J., Zsoter, E., Buontempo, C.,
529 and Thépaut, J.-N.: ERA5-Land: a state-of-the-art global reanalysis dataset for land applications, *Earth System Science Data*,
530 13, 4349-4383, 10.5194/essd-13-4349-2021, 2021.
- 531 Myneni, R., Knyazikhin, Y., Park, T.: MCD15A2H MODIS/Terra+Aqua Leaf Area Index/FPAR 8-day L4 Global 500m SIN
532 Grid V006 [dataset], <https://doi.org/10.5067/MODIS/MCD15A2H.006>, 2015.
- 533 Nilson, T.: A theoretical analysis of the frequency of gaps in plant stands, *Agricultural Meteorology*, 8, 25-38, 1971.
- 534 Norman, J. M. and Campbell, G. S.: Canopy structure, in: *Plant Physiological Ecology: Field methods and instrumentation*,
535 edited by: Pearcy, R. W., Ehleringer, J. R., Mooney, H. A., and Rundel, P. W., Springer Netherlands, Dordrecht, 301-325,
536 10.1007/978-94-009-2221-1_14, 1989.
- 537 Pisek, J. and Adamson, K.: Dataset of leaf inclination angles for 71 different Eucalyptus species, *Data Brief*, 33, 106391,
538 10.1016/j.dib.2020.106391, 2020.
- 539 Pisek, J., Ryu, Y., and Alikas, K.: Estimating leaf inclination and G-function from leveled digital camera photography in
540 broadleaf canopies, *Trees*, 25, 919-924, 10.1007/s00468-011-0566-6, 2011.
- 541 Pisek, J., Sonnentag, O., Richardson, A. D., and Möttus, M.: Is the spherical leaf inclination angle distribution a valid
542 assumption for temperate and boreal broadleaf tree species?, *Agricultural and Forest Meteorology*, 169, 186-194,
543 10.1016/j.agrformet.2012.10.011, 2013.
- 544 Pisek, J., Diaz-Pines, E., Matteucci, G., Noe, S., and Rebmann, C.: On the leaf inclination angle distribution as a plant trait
545 for the most abundant broadleaf tree species in Europe, *Agricultural and Forest Meteorology*, 323,
546 10.1016/j.agrformet.2022.109030, 2022.



- 547 Raabe, K., Pisek, J., Sonnentag, O., and Annuk, K.: Variations of leaf inclination angle distribution with height over the
548 growing season and light exposure for eight broadleaf tree species, *Agricultural and Forest Meteorology*, 214-215, 2-11,
549 10.1016/j.agrformet.2015.07.008, 2015.
- 550 Ross, J.: Radiative transfer in plant communities, *Vegetation and the Atmosphere*, 13-55, 1975.
- 551 Ross, J.: The radiation regime and architecture of plant stands, 3, Springer Science & Business Media 1981.
- 552 Ryu, Y., Sonnentag, O., Nilson, T., Vargas, R., Kobayashi, H., Wenk, R., and Baldocchi, D. D.: How to quantify tree leaf
553 area index in an open savanna ecosystem: A multi-instrument and multi-model approach, *Agricultural and Forest*
554 *Meteorology*, 150, 63-76, 10.1016/j.agrformet.2009.08.007, 2010.
- 555 Schaaf, C. and Wang, Z.: MCD43A1 MODIS/Terra+Aqua BRDF/Albedo Model Parameters Daily L3 Global - 500m V006,
556 NASA EOSDIS Land Processes Distributed Active Archive Center [dataset],
557 <https://doi.org/10.5067/MODIS/MCD43A1.006>, 2015a.
- 558 Schaaf, C. and Wang, Z.: MCD43A4 MODIS/Terra+Aqua BRDF/Albedo Nadir BRDF Adjusted Ref Daily L3 Global -
559 500m V006, NASA EOSDIS Land Processes Distributed Active Archive Center [dataset],
560 <https://doi.org/10.5067/MODIS/MCD43A4.006>, 2015b.
- 561 Sellers, P. J.: Canopy reflectance, photosynthesis and transpiration, *International Journal of Remote Sensing*, 6, 1335-1372,
562 10.1080/01431168508948283, 1985.
- 563 Shen, R., Dong, J., Yuan, W., Han, W., Ye, T., and Zhao, W.: A 30-m Resolution Distribution Map of Maize for China
564 Based on Landsat and Sentinel Images, *Journal of Remote Sensing*, 2022, doi:10.34133/2022/9846712, 2022.
- 565 Stadt, K. J. and Lieffers, V. J.: MIXLIGHT: a flexible light transmission model for mixed-species forest stands, *Agricultural*
566 *and Forest Meteorology*, 102, 235-252, 2000.
- 567 Sulla-Menashe, D., Gray, J. M., Abercrombie, S. P., and Friedl, M. A.: Hierarchical mapping of annual global land cover
568 2001 to present: The MODIS Collection 6 Land Cover product, *Remote Sens. Environ.*, 222, 183-194,
569 10.1016/j.rse.2018.12.013, 2019.
- 570 Tadono, T., Ishida, H., Oda, F., Naito, S., Minakawa, K., and Iwamoto, H.: Precise global DEM generation by ALOS
571 PRISM, *ISPRS Annals of the Photogrammetry, Remote Sensing and Spatial Information Sciences*, 2, 71-76, 2014.
- 572 Tang, H., Ganguly, S., Zhang, G., Hofton, M. A., Nelson, R. F., and Dubayah, R.: Characterizing leaf area index (LAI) and
573 vertical foliage profile (VFP) over the United States, *Biogeosciences*, 13, 239-252, 10.5194/bg-13-239-2016, 2016.
- 574 Toda, M., Ishihara, M. I., Doi, K., and Hara, T.: Determination of species-specific leaf angle distribution and plant area
575 index in a cool-temperate mixed forest from UAV and upward-pointing digital photography, *Agricultural and Forest*
576 *Meteorology*, 325, 10.1016/j.agrformet.2022.109151, 2022.
- 577 Utsugi, H., Araki, M., Kawasaki, T., and Ishizuka, M.: Vertical distributions of leaf area and inclination angle, and their
578 relationship in a 46-year-old *Chamaecyparis obtusa* stand, *For. Ecol. Manage.*, 225, 104-112,
579 <https://doi.org/10.1016/j.foreco.2005.12.028>, 2006.



- 580 van Zanten, M., Pons, T. L., Janssen, J. A. M., Voeselek, L. A. C. J., and Peeters, A. J. M.: On the Relevance and Control of
581 Leaf Angle, *Crit. Rev. Plant Sci.*, 29, 300-316, 10.1080/07352689.2010.502086, 2010.
- 582 Wang, Y. and Fang, H.: Estimation of LAI with the LiDAR Technology: A Review, *Remote Sensing*, 12,
583 10.3390/rs12203457, 2020.
- 584 Weiss, M. and Baret, F.: CAN-EYE V6.4.91 User Manual, [https://www6.paca.inrae.fr/can-](https://www6.paca.inrae.fr/can-eye/Documentation/Documentation)
585 [eye/Documentation/Documentation](https://www6.paca.inrae.fr/can-eye/Documentation/Documentation), 2017.
- 586 Wilson, J.: Inclined point quadrats, *New Phytol.*, 59, 1-7, 10.1111/j.1469-8137.1960.tb06195.x, 1960.
- 587 Wilson, J. W.: Analysis of the spatial distribution of foliage by two-dimensional point quadrats, *New Phytol.*, 58, 92-99,
588 <https://doi.org/10.1111/j.1469-8137.1959.tb05340.x>, 1959.
- 589 Xiao, Q., McPherson, E. G., Ustin, S. L., and Grismer, M. E.: A new approach to modeling tree rainfall interception, *Journal*
590 *of Geophysical Research: Atmospheres*, 105, 29173-29188, 2000.
- 591 Yan, G., Jiang, H., Luo, J., Mu, X., Li, F., Qi, J., Hu, R., Xie, D., and Zhou, G.: Quantitative Evaluation of Leaf Inclination
592 Angle Distribution on Leaf Area Index Retrieval of Coniferous Canopies, *Journal of Remote Sensing*, 2021, 1-15,
593 10.34133/2021/2708904, 2021.
- 594 You, N., Dong, J., Huang, J., Du, G., Zhang, G., He, Y., Yang, T., Di, Y., and Xiao, X.: The 10-m crop type maps in
595 Northeast China during 2017-2019, *Sci Data*, 8, 41, 10.1038/s41597-021-00827-9, 2021.
- 596 Zhao, J., Li, J., Liu, Q., Xu, B., Yu, W., Lin, S., and Hu, Z.: Estimating fractional vegetation cover from leaf area index and
597 clumping index based on the gap probability theory, *International Journal of Applied Earth Observation and Geoinformation*,
598 90, 102-112, 10.1016/j.jag.2020.102112, 2020.
- 599 Zheng, G. and Moskal, L. M.: Leaf orientation retrieval from terrestrial laser scanning (TLS) data, *IEEE Transactions on*
600 *Geoscience and Remote Sensing*, 50, 3970-3979, 10.1109/TGRS.2012.2188533, 2012.
- 601 Zou, X. and Möttus, M.: Retrieving crop leaf tilt angle from imaging spectroscopy data, *Agricultural and Forest Meteorology*,
602 205, 73-82, 10.1016/j.agrformet.2015.02.016, 2015.
- 603
- 604